current issues in molecular biology

MDPI

Article

From Scar-Free Skin Repair in Leopard Geckos to Ligand-Dependent Reorganization at the Human KEAP1–NRF2 Interface

Yian Li [1], Jianlin Li [1], Dong-Qing Wei [1], Wei Miao [2,*] and Jiayi Li [1,*]

[1] Joint International Research Laboratory of Metabolic & Developmental Sciences, School of Life Sciences and Biotechnology, Shanghai Jiao Tong University, Shanghai 200040, China; yianli2026@163.com (Y.L.); jianlinli@sjtu.edu.cn (J.L.); dqwei@sjtu.edu.cn (D.-Q.W.)
[2] McCormick School of Engineering, Northwestern University, Evanston, IL 60208, USA
* Correspondence: drmiaowei@163.com (W.M.); jemmylee@sjtu.edu.cn (J.L.)

Abstract

The human Kelch-like ECH-associated protein 1 (KEAP1)–nuclear factor erythroid 2-related factor 2 (NRF2) interface is a target for modulating redox signaling through small-molecule recognition. Motivated by scar-free skin repair in leopard geckos, we examined human KEAP1 ligand recognition and compared recognition-site sequences with predicted leopard-gecko orthologs. Replicated molecular dynamics simulations compared wild-type and Q530A human KEAP1 in apo and C1–C3-bound states. C2, modeled in its dianionic state, redistributed recognition from R483 toward R415: the mean R415-only fraction increased from 0.036 to 0.627, with ring nitrogen atoms and the deprotonated sulfonamide nitrogen supporting the new contacts. This redistribution accompanied a large carboxylate displacement, while mean distal coverage remained similar. Additional C2 monoanion simulations sampled different R415/R483 contact states and distal coverage, with between-trajectory and time-window variation. C3 retained local R483 recognition but showed pronounced distal reorganization. Among R483-contacting frames, G81/E82 coverage decreased from 0.554 ± 0.188 to 0.084 ± 0.026. The principal dianionic C2 contact and C3 conditional-coverage contrasts retained their directions across predefined time windows and trajectory-omission analyses. Together, these results identify contact redistribution and distal reorganization with retained local recognition as distinct responses at the KEAP1–NRF2 interface, providing experimentally testable structural hypotheses for ligand recognition.

Keywords: KEAP1; NRF2; leopard gecko; molecular dynamics; scar-free skin repair; ligand recognition

Check for updates

Academic Editor: Sung-whan Kim

Received: 9 October 2026
Revised: 12 November 2026
Accepted: 19 November 2026
Published: 23 November 2026

Copyright: © 2026 by the authors. Licensee MDPI, Basel, Switzerland. This article is an open access article distributed under the terms and conditions of the Creative Commons Attribution (CC BY) license.

1. Introduction

Scar-free cutaneous repair offers a distinctive biological perspective on vertebrate wound healing. In leopard geckos (*Eublepharis macularius*), full-thickness excisional wounds on both the tail and body heal without fibrotic scarring [1]. This process combines relatively rapid re-epithelialization with delayed vascular development and collagen deposition, rather than the exuberant vascular response commonly associated with scar-forming repair [1]. Such findings suggest that the timing and organization of tissue responses are as important as wound closure itself. Yet the molecular regulators that enable this phenotype remain incompletely understood. The leopard gecko therefore provides a compelling biological motivation for studying molecular pathways that may shape cutaneous repair, while care

is required to not infer pathway causality from the phenotype alone. Among the redox-regulatory pathways implicated in mammalian wound repair, KEAP1–NRF2 signaling offers a molecular target for further study [2,3].

Kelch-like ECH-associated protein 1 (KEAP1) promotes the turnover of nuclear factor erythroid 2-related factor 2 (NRF2), a transcription factor that coordinates cellular responses to oxidative stress. In diabetic wound models, local Keap1 suppression restored redox homeostasis and accelerated wound closure [2]. Complementary experiments showed delayed diabetic wound healing with Nrf2 deficiency and improved repair following NRF2 activation [3]. Sustained epidermal NRF2 activation, however, can disrupt barrier function and produce hyperkeratosis and inflammation [4]. Together, these findings motivate the investigation of KEAP1 recognition as a molecular basis for pathway modulation, whose consequences for skin depend on the biological context and duration of activation.

Motivated by this biological context, we examined ligand recognition using human KEAP1 models and three computationally selected compounds, C1–C3; the leopard-gecko sequences provide a comparative context. Figure 1 introduces the recognition interface and the simulated chemical species, alongside human–leopard-gecko sequence correspondence at the principal recognition sites.

The human KEAP1 Kelch domain forms a six-bladed β-propeller whose recognition surface contains polar, charged and hydrophobic regions that accommodate the acidic NRF2 ETGE motif [5]. This interaction is a target for noncovalent protein–protein interaction inhibitors, and experiments distinguish the contributions of ETGE and DLG engagement to the larger regulatory complex [6]. Small-molecule recognition at this surface involves both local residue contacts and placement across the extended NRF2-binding region.

Crystallographic and biochemical studies have established several classes of noncovalent KEAP1 ligands [7–10]. Crystallography and molecular dynamics (MD) have revealed multiple binding modes, including differences between crystal poses and solution trajectories [11]. Structural and energetic mapping identifies alternative R415 orientations and neighboring interaction regions [12], while macrocycle optimization highlights receptor flexibility and local hydration [13]. Previous simulations have also examined interaction energetics and ligand separation [14]. This work provides a framework for examining how local contact patterns relate to broader ligand placement.

A specific structural question is whether retention of a local recognition contact accompanies maintained occupation of the wider NRF2-binding region. Ligand motion can combine internal deformation, repositioning and withdrawal from part of the interface. Linking direct hydrogen-bond states to the coverage of fixed ETGE reference sites in the same frames resolves the relationship between these local and regional responses.

Crystallographic fragment complexes show polar contacts involving Q530 [12]. Here, we used Q530A as a defined perturbation of the KEAP1 recognition environment and compared apo and C1–C3-bound systems. The three candidates were selected from distinct generic molecular cores through receptor-ensemble screening. By combining same-frame contact-state analysis with ETGE reference-site coverage, we asked whether local recognition and broader ligand placement change together or become uncoupled. This comparison revealed two distinct responses: the redistribution of dianionic C2 contacts toward R415 and the loss of C3 distal coverage despite retained R483 recognition.

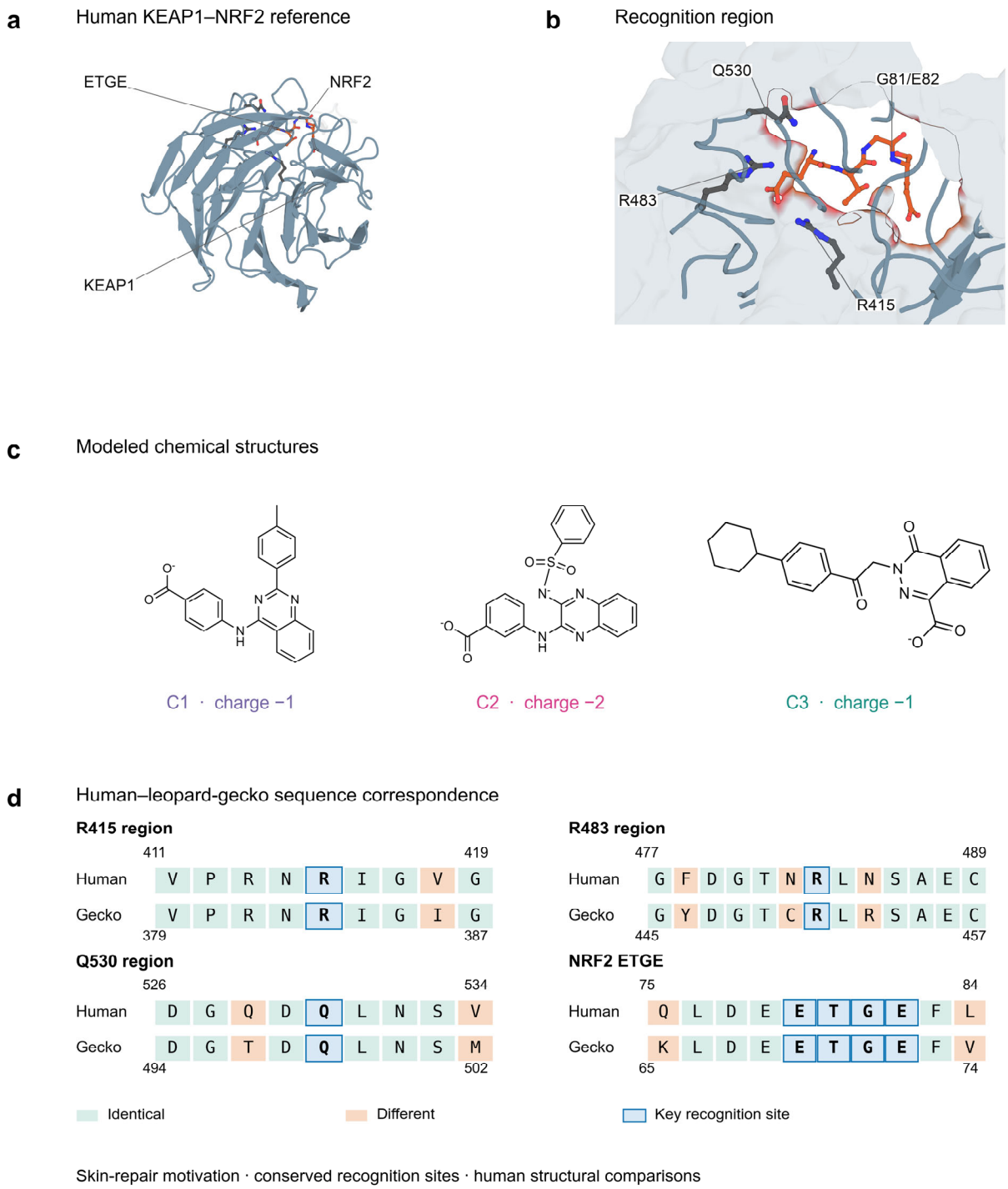


Figure 1. Molecular context and sequence correspondence. (**a**) Human KEAP1–NRF2 reference. (**b**) R415, R483 and Q530 around the ETGE recognition region. (**c**) C1, dianionic C2 and C3 in their original simulated microstates; the C2 monoanion is specified in Table S1. (**d**) Local human–leopard-gecko alignments; blue outlines mark principal recognition sites. The complete studied-region alignment is shown in Figure S11. In (**a**,**b**), human KEAP1 is blue-gray and the NRF2 reference is orange; the semitransparent surface in (**b**) depicts the KEAP1 recognition region.

2. Materials and Methods

2.1. Structural Systems and Evidence Sources

Core models comprised human WT and Q530A KEAP1 (UniProt Q14145, residues 325–609) in apo and C1-, C2- or C3-bound states. C1–C3 were selected from an ensemble

screen (Section 2.6; Table S1). Structural references were PDB 6TYM–08A [8], 2FLU–NRF2 peptide [5], 7Q8R–63 and 7Q96–64 [13], and 4IQK–IQK [7]. Labels 08A and IQK are PDB chemical-component identifiers; 63 and 64 are publication compound numbers. Known-ligand poses were transferred to a common 6TYM-derived receptor, and the NRF2 reference peptide comprised residues 69–84.

Each of the eight core conditions contributed three 200 ns production trajectories (24 trajectories; 4.8 μs). The simulated formal charges of C1, C2 and C3 were −1, −2 and −1, respectively. C2 was modeled as a dianion with deprotonated carboxylate and sulfonamide nitrogen.

For protonation-state sensitivity, an additional C2 monoanion was simulated with WT and Q530A KEAP1 in three independently velocity-seeded 200 ns production trajectories per receptor (six trajectories; 1.2 μs). The carboxylate remained deprotonated and the sulfonamide nitrogen was protonated. The original core cohort together with these sensitivity simulations comprised 30 trajectories and 6.0 μs of production sampling.

2.2. Molecular Dynamics and Sampling

Protein and peptide parameters used ff14SB [15]; ligands used GAFF2, AM1-BCC charges and supplementary terms from parmchk2 [16,17]. Histidines were HIE, cysteines were reduced CYS, and truncated termini were charged. Rectangular TIP3P boxes extended 12 Å beyond the solute and contained neutralizing ions plus approximately 0.15 M NaCl, using TIP3P-specific Joung–Cheatham ion parameters. Exact microstates and preparation settings are given in Supplementary Methods SM1.

Amber 26 GPU PMEMD simulations used a 2 fs timestep, SHAKE constraints on bonds involving hydrogen (ntc = 2; ntf = 2), particle-mesh Ewald electrostatics and a 9 Å direct-space cutoff. Langevin temperature control was maintained 298.15 K with a collision frequency of 2 ps−1, and isotropic Monte Carlo pressure control was maintained at 1 bar. Two minimizations preceded 100 ps heating, 500 ps density relaxation and 1 ns unrestrained equilibration. Trajectories within each condition shared prepared coordinates and topology but used different heating velocity seeds. Coordinates were saved every 10 ps. The production time excludes the preceding 1.6 ns preparation interval.

All three candidate poses used receptor B1_10, an actual frame at 47.31 ns of macrocycle-63 reference trajectory 3 and the member nearest a reference-ensemble cluster center. WT apo was generated by ligand removal, and Q530A was introduced into the corresponding apo and holo starts. WT candidate runs continued from 100 to 200 ns at the same trajectories. Core analyses used 20–200 ns; equal-duration 20–100 and 120–200 ns windows assessed time sensitivity. Separate peptide and known-ligand comparisons used 20–100 ns. Receptor selection and the reference cohort are detailed in Supplementary Methods SM5. In the screening records, the representative selected poses of all three candidates were associated with B1_10; the shared receptor therefore reflects the selected poses rather than a separate claim of universal optimality. Following mutation introduction, each Q530A system underwent the minimization, heating, density relaxation and equilibration stages described above before production.

The monoanion was mapped to the original selected C2 pose, preserving the protein and ligand heavy-atom starting coordinates and adding a hydrogen to the sulfonamide nitrogen. Its GAFF2 atom types, AM1-BCC charges and supplementary parameters were assigned for this microstate. WT and Q530A complexes were independently solvated, neutralized, minimized, heated and equilibrated using the same protocol and analysis windows.

2.3. Coordinates and Complementary Measures of Ligand Motion

Trajectories were imaged with CPPTRAJ [18] and sampled every 100 ps. All 285 receptor Cα atoms were fitted to a common 6TYM-derived frame. Protein Cα RMSD used the prepared WT apo reference, and RMSF used each trajectory's mean coordinates. The radius of gyration used all protein atoms and topology masses. Common-pocket RMSD used 229 heavy-atom identities shared by WT and Q530A in a predefined interface mask. The relative geometric contrast was the Q530A–WT difference in a holo-observable minus the corresponding apo difference (Supplementary Methods SM2).

Whole-ligand heavy-atom RMSD and centroid displacement described motion from the prepared pose in the receptor frame; self-fitted ligand RMSD described internal deformation. Ring-core and peripheral atom sets resolved regional displacement. The C/O/O carboxylate centroid tracked the anchoring group; this measure was undefined for IQK. For the peptide, ETGE residues 79–82 defined the core.

2.4. ETGE Reference-Site Coverage and Sensitivity Analyses

The aligned 2FLU-derived peptide supplied 29 fixed ETGE79–82 heavy-atom reference sites. ETGE reference-site coverage was the fraction within 3 Å of any ligand heavy atom, counting each site once. Distal reference-site coverage pooled the 13 G81/E82 sites with equal weight per atom. The reference peptide was absent from the small-molecule simulations.

Whole-ETGE descriptor checks varied the distance cutoff, receptor-fit selection, peptide conformation and included atom sets (Figure S5; Supplementary Methods SM2). The targeted C3 R483-conditioned distal comparison was assessed separately across time windows and trajectory omissions.

2.5. Solvent Exposure, Contact States and Local Geometry

Ligand solvent-accessible surface area was determined using MDTraj's Shrake–Rupley implementation, a 1.4 Å probe and 960 surface points per atom [19]. Each holo trajectory contributed 180 observations at 1 ns spacing over the primary window. All solute atoms blocked accessibility, but only ligand areas were summed. The buried fraction was one minus the bound-to-isolated area ratio for the same ligand conformation.

Chemically typed N/O hydrogen bonds required a donor–acceptor distance $\leq$3.5 Å and donor–hydrogen–acceptor angle $\geq$135°. Per-residue occupancy counted a frame once if any qualifying atom pair was present. A single-water bridge required the same water molecule to satisfy both protein–water and water–ligand criteria in that frame.

Hydrogen-bond donor and acceptor assignments were evaluated separately for the C2 microstates, and direct events were filtered before residue-level and functional-group unions were calculated. The protonated sulfonamide nitrogen was treated as a donor rather than an acceptor.

Each holo-frame was classified as R483 only, R415 only, both or neither. Functional-group occupancies retained overlapping and simultaneous events. Conditional distal coverage was calculated within each trajectory using R483-present frames, and then averaged with equal trajectory weights. R483–carboxylate hydrogen bonding supplied a stricter condition; WT C3 was also partitioned by Q530 hydrogen bonding.

R415/R483 orientation used the Cα–Cζ axis relative to prepared WT apo. Ligand orientation used the carboxylate-to-ring axis relative to the direction toward the distal reference centroid. Local water counts used periodic minimum-image distances within 4 Å of residue-530 Cβ (5 Å sensitivity check) and within 3.5 Å of each arginine guanidinium center, sampled every 1 ns. These shared regions enabled apo/holo and WT/Q530A comparisons.

2.6. Candidate Screening and Retrospective Pose Evaluation

C1–C3 originated from the NCI NExT Diversity 3500 Pilot Set and correspond to NSC2518124, NSC2530227 and NSC2532809, respectively. Epik [20] and ETKDGv3 [21] supplied microstates and conformers for AutoDock 4.2.6 screening [22]; Morgan fingerprints described chemical similarity [23]. An ensemble of 12 receptor frames and eight occupancy-weighted pharmacophore templates supported candidate selection before MD. Library preparation, clustering, pharmacophore tolerances and selection rules are specified in Supplementary Methods SM5.

Retrospective pose evaluation compared static, expanded static and ensemble searches with pharmacophore reranking. Four development compounds and eight related external crystallographic ligands were evaluated with three search seeds per compound. Recovery was defined by symmetry-corrected RMSD $\leq$2 Å against the transferred experimental pose. Full search settings and recovery results are provided in Supplementary Methods SM5 and Figure S10.

2.7. Statistical Summaries, Molecular Illustrations and Endpoint Energies

Trajectories were the statistical units ($n = 3$ per condition), and WT/Q530A groups were unpaired. Means and sample SD were calculated from equally weighted trajectory summaries [24]. Distributions and conditional subsets assigned equal total weight to each trajectory; boxes show weighted medians and interquartile ranges, with whiskers extending to observations within 1.5 interquartile ranges. Leave-one-trajectory-out analysis omitted one trajectory from its own group while retaining all three in the other group. Summaries were descriptive, without frame-level significance tests. Conditional-subset handling and sensitivity procedures are specified in Supplementary Methods SM4.

PyMOL illustrated representative structures from contact-defined sub-ensembles in the common receptor frame. C2 examples represented WT R483-only and Q530A R415-only recognition; C1/C3 examples represented R483-contacting configurations. The representative-frame algorithm and panel-specific conditions are detailed in Supplementary Methods SM3. ChemDraw 26 supplied the chemical drawings, with RDKit checks of chemical identity and formal charge.

MM/PBSA and MM/GBSA estimates used MMPBSA.py with the AmberTools 26 Sander backend [25]. Each holo trajectory contributed 180 snapshots at 1 ns spacing over 20.01–199.01 ns; receptor and ligand coordinates were extracted from the same complex snapshots. Both models used mbondi2 radii, dielectric constants 1 and 80, and 0.15 M salt, with entropy omitted. The nonpolar models for GB residue decomposition and the GB total, together with all PB/GB settings, are specified in Supplementary Methods SM4. Because configurational entropy was omitted, these endpoint estimates are not complete binding free energies or quantitative predictions of binding affinity.

The same matched-snapshot endpoint protocol was applied to each additional C2 monoanion trajectory.

2.8. Human–Leopard-Gecko Sequence Comparison

Predicted full-length leopard-gecko KEAP1 and NRF2 proteins were retrieved from NCBI RefSeq [26], and reviewed human reference sequences were obtained from UniProtKB [27]. NCBI Ortholog assignments linked the gecko genes to human KEAP1 and NFE2L2. Global BLOSUM62 alignments used Biopython [28], with gap-opening and extension scores of −10 and −0.5. Residue mappings were checked at −12/−0.5 and −10/−1. Comparisons covered the modeled human KEAP1 segment, the predefined interface mask and the NRF2 reference-peptide region. Accessions and mapped positions are given in Table S5.

3. Results

3.1. WT Recognition and Apo Pocket Response Establish the Structural Background

Global backbone descriptors remained similar across systems, with the radius of gyration near 17.9 Å throughout the sampled trajectories (Figures S1–S3). We therefore compared local ligand recognition and the apo pocket response (Figures 2 and 3).

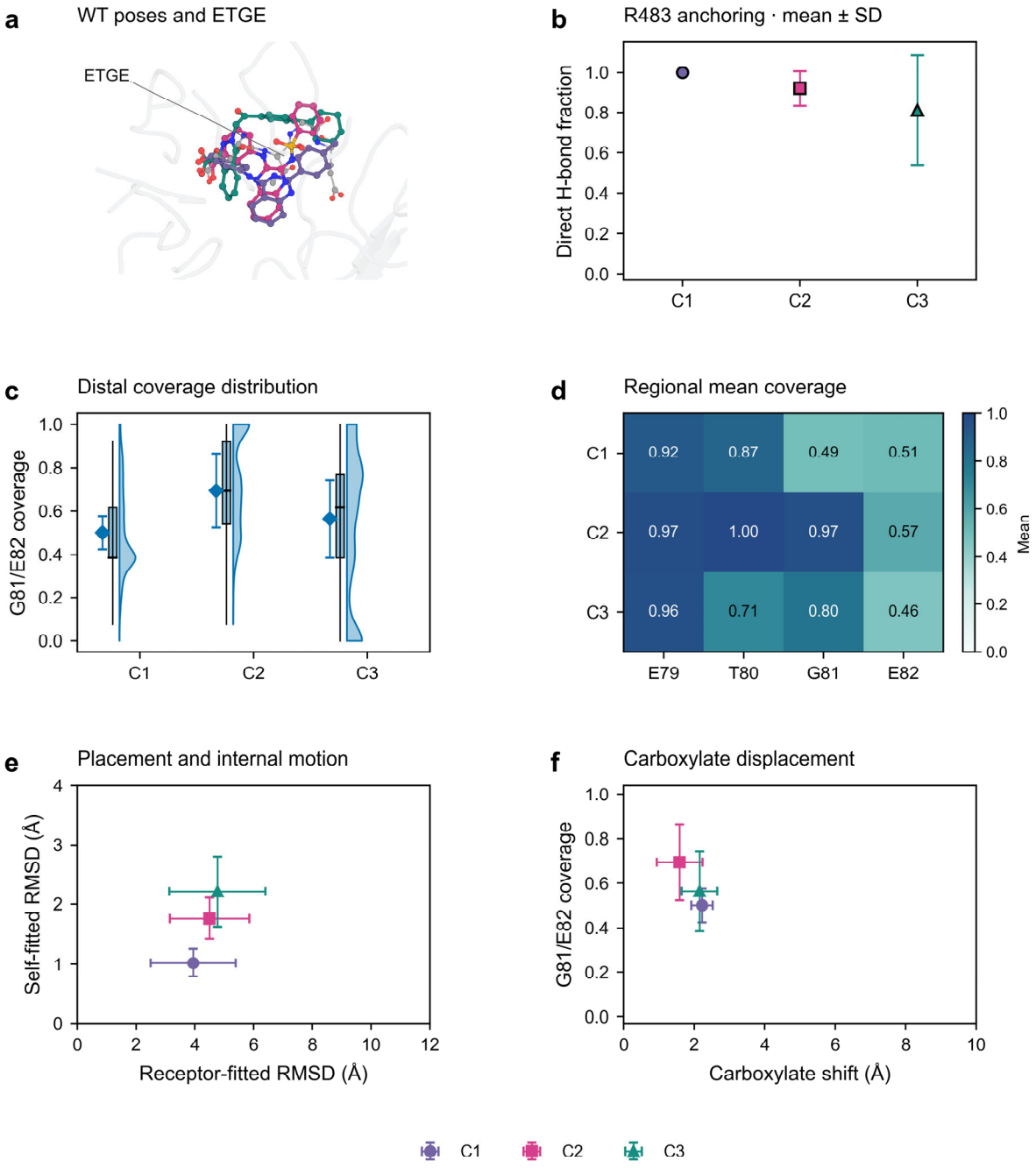


Figure 2. WT ligand recognition and spatial coverage. (**a**) Representative C1–C3 poses with the gray ETGE reference. (**b**) R483 hydrogen-bond occupancy. (**c**) Distal G81/E82 coverage. (**d**) Coverage of individual ETGE residues. (**e**) Receptor-fitted and self-fitted ligand RMSD. (**f**) Carboxylate-centroid displacement and distal coverage. Symbols and error bars show means and between-trajectory SD ($n = 3$ trajectories per condition).

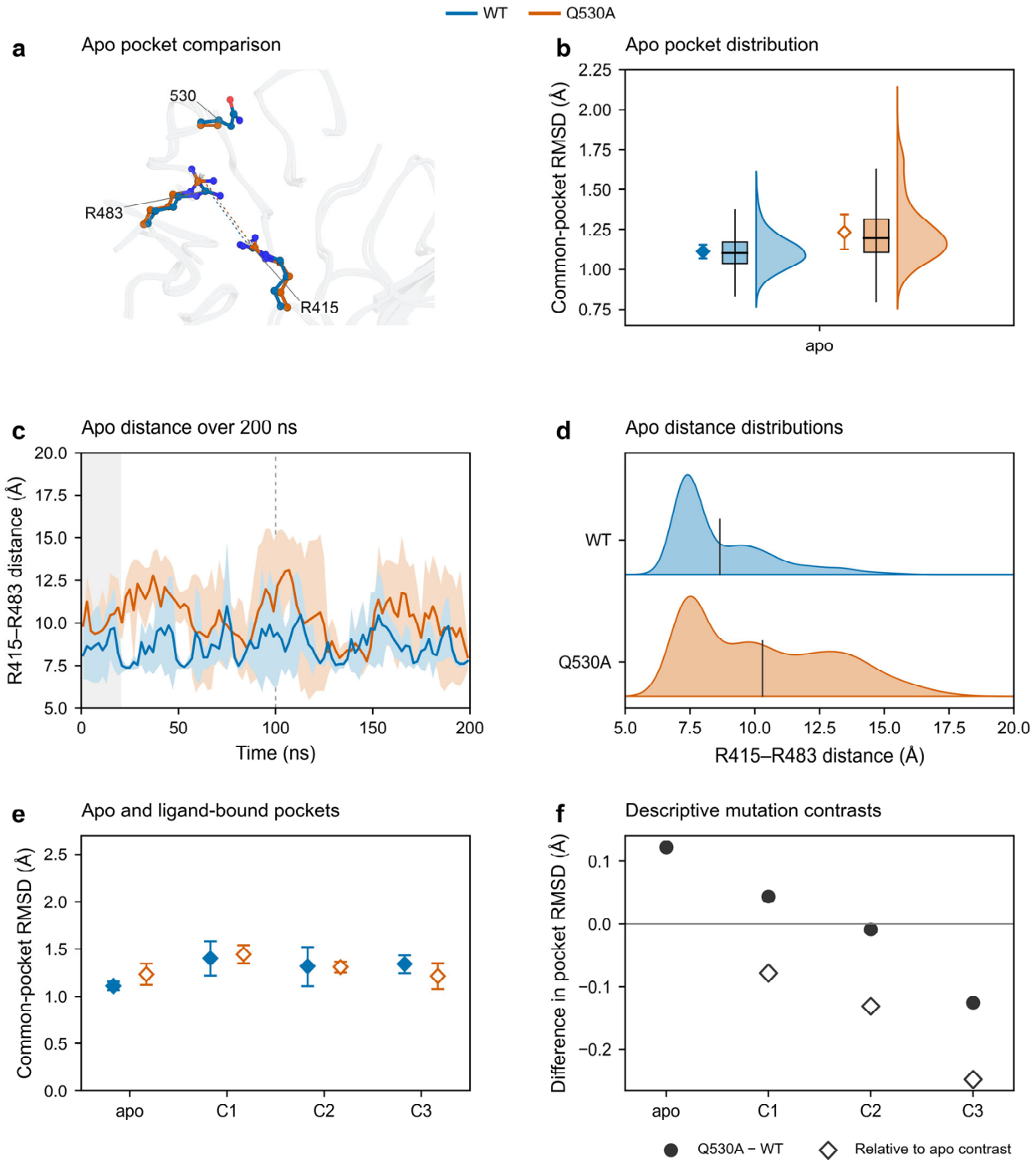


Figure 3. Apo and ligand-bound pocket geometry. (**a**) WT and Q530A apo structures showing the R415–R483 separation. (**b**) Apo pocket RMSD. (**c**,**d**) Apo R415–R483 distance over time and its distribution. (**e**) Common-pocket RMSD across conditions. (**f**) Q530A–WT geometric differences and relative geometric contrasts against apo. Error bars and shading show between-trajectory SD ($n = 3$ trajectories per condition).

In WT KEAP1, mean R483 direct hydrogen-bond occupancies were 1.000, 0.920 and 0.811 for C1, C2 and C3, respectively (Figure 2b). Corresponding distal G81/E82 coverages were 0.500, 0.693 and 0.564 (Figure 2c). Thus, all three ligands frequently contacted R483 while occupying different extents of the distal reference region. C2 covered G81 more extensively than E82, whereas C1 covered the two regions at similar fractions (Figure 2d).

Receptor-fitted ligand RMSDs exceeded self-fitted RMSDs, indicating that ligand motion combined repositioning with internal deformation (Figure 2e). Carboxylate-centroid

displacement resolved the movement of the local anchoring group (Figure 2f). The motion, burial and whole-ETGE comparisons further described the distinct spatial distributions of the three ligands (Figures S4 and S5).

Separate peptide and known-ligand trajectories provided a reference for this spatial variation (Figure S9). The peptide flanks moved while the ETGE core remained close to its reference placement. Macrocycles 63 and 64 both retained broad ETGE reference-site coverage despite their different reported affinities [13], showing that similar regional placement occurred across ligands with distinct experimental affinities.

Apo Q530A showed greater mean pocket displacement and separation of the two arginines compared to WT (Figure 3). Common-pocket RMSD increased from 1.11 ± 0.04 to 1.23 ± 0.11 Å, and the R415–R483 guanidinium-centroid distance increased from 8.65 ± 0.22 to 10.29 ± 1.19 Å. Relative geometric contrasts showed ligand-dependent shifts in the pocket response against this apo background (Figure 3e,f).

Q530A increased local water access around residue 530 in both apo and ligand-bound systems (Figure S6). Within 4 Å of residue-530 Cβ, mean water counts changed from 0.07 to 1.11 in apo, from 0.11 to 0.75 for C2 and from 0.12 to 0.68 for C3; the same direction was observed with a 5 Å radius. A shared hydration response therefore accompanied the distinct ligand-recognition patterns described below.

3.2. C2 Contact Redistribution and Protonation-State Sensitivity

C2 in its simulated dianionic state shifted from predominantly R483-centered recognition in WT toward R415-centered recognition in Q530A (Figure 4). Mean R483 occupancy decreased from 0.920 ± 0.086 to 0.235 ± 0.238. The R483-only fraction decreased from 0.861 ± 0.067 to 0.179 ± 0.202, while the R415-only fraction increased from 0.036 ± 0.054 to 0.627 ± 0.183 (Figure 4c; Table S4). R415-only and R483-only runs alternated within the Q530A trajectories, indicating redistribution among contact states.

The R415-centered pattern recruited C2 ring nitrogen atoms and the deprotonated sulfonamide nitrogen (Figure 4a,b,d). In Q530A, mean R415 occupancies were 0.598 ± 0.188 for ring nitrogen and 0.618 ± 0.183 for sulfonamide nitrogen, compared with 0.122 ± 0.080 for the carboxylate. Both nitrogen groups contacted R415 simultaneously in a fraction of 0.579 ± 0.180, compared with 0.022 ± 0.038 in WT. Recognition therefore shifted to a different region of the ligand as the predominant arginine partner changed.

The carboxylate-centroid displacement increased from 1.59 ± 0.65 Å in WT to 8.06 ± 2.79 Å in Q530A, while mean distal coverage changed from 0.693 ± 0.171 to 0.657 ± 0.166 (Table S2). Together, these observations define a contact-redistribution mode in which C2 reorganizes its anchoring network from R483 toward R415 while largely retaining distal coverage of the ETGE reference region.

C1 showed a smaller response: R483 hydrogen-bond occupancy remained near unity, and distal coverage changed from 0.500 ± 0.075 to 0.462 ± 0.057 (Figure 4e; Table S2). Against this comparison, the C2 response identifies an alternative anchoring pattern built around R415 recognition by its nitrogen-containing region.

The additional C2 monoanion simulations sampled a different distribution of contact combinations (Figure 4c,d; Figures S13–S15 and S17). In WT, simultaneous R415/R483 hydrogen bonds occupied 0.609 ± 0.324 of sampled frames for the monoanion and 0.059 ± 0.038 for the dianion. Corresponding G81/E82 reference-site coverages were 0.349 ± 0.080 and 0.693 ± 0.171. In Q530A, simultaneous-contact fractions were 0.325 ± 0.311 and 0.055 ± 0.053, with coverages of 0.449 ± 0.091 and 0.657 ± 0.166 for the monoanion and dianion, respectively. Monoanion trajectories showed substantial contact-state variation across repeats and time windows. No R415–sulfonamide-nitrogen hydrogen bond was observed in the monoanion primary-window frames, whereas Q530A dianion occupancy

was 0.618 ± 0.183. Thus, the sampled recognition network changed with the modeled C2 microstate.

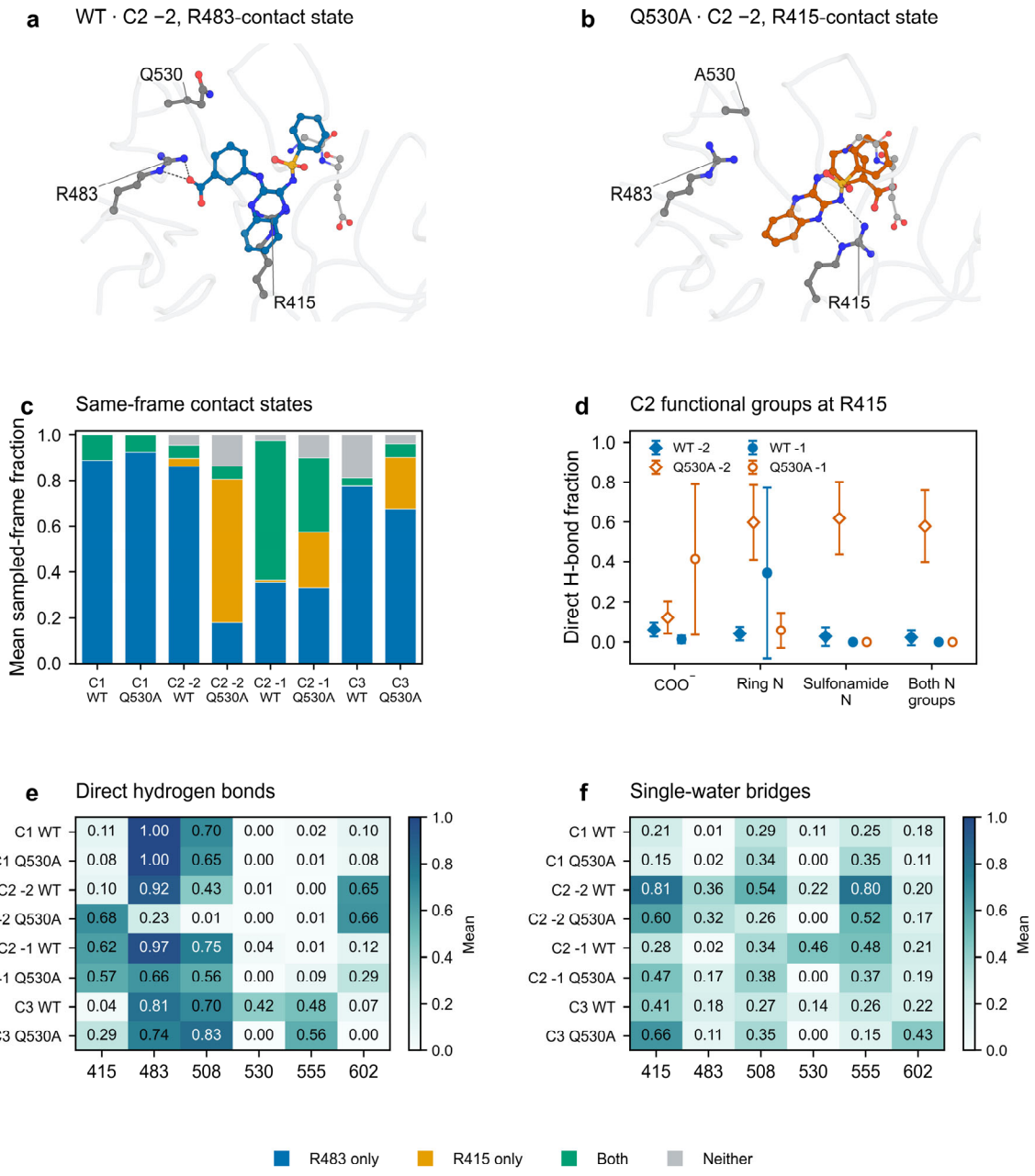


Figure 4. C2 contact redistribution and functional-group recognition. (**a**,**b**) Representative structures of the C2 dianion, illustrating R483-centered recognition in WT and R415-centered recognition in Q530A; the G81/E82 portion of the ETGE reference is shown as gray-carbon ball-and-stick, with heteroatoms colored by element; dashed lines indicate hydrogen bonds. (**c**) R483-only, R415-only, both-contact and neither-contact states for the original C1–C3 conditions and additional C2 monoanion conditions. (**d**) C2 functional-group contacts with R415 in both microstates; "Both N groups" denotes simultaneous ring-nitrogen and sulfonamide-nitrogen contacts. (**e**,**f**) Direct hydrogen-bond and single-water bridge occupancies for the same conditions. Summaries use the 20–200 ns window and equal trajectory weights; error bars show between-trajectory SD ($n = 3$ per condition). C2 −2 and C2 −1 denote the dianion and monoanion, respectively.

3.3. C3 Loses Distal Coverage Despite Retaining R483 Recognition

C3 showed a different combination of local and regional changes (Figure 5). R483 hydrogen-bond occupancy remained high on average, changing from 0.811 ± 0.273 in WT to 0.736 ± 0.374 in Q530A (Figure 4e). Carboxylate-centroid displacement was similar in magnitude, at 2.15 ± 0.50 and 2.24 ± 0.56 Å, respectively. In contrast, receptor-fitted ligand RMSD increased from 4.77 ± 1.64 to 7.79 ± 0.97 Å, while unconditional distal coverage decreased from 0.564 ± 0.179 to 0.086 ± 0.056 (Table S2). This pattern was consistent with a greater reorganization of ligand regions beyond the retained local anchor.

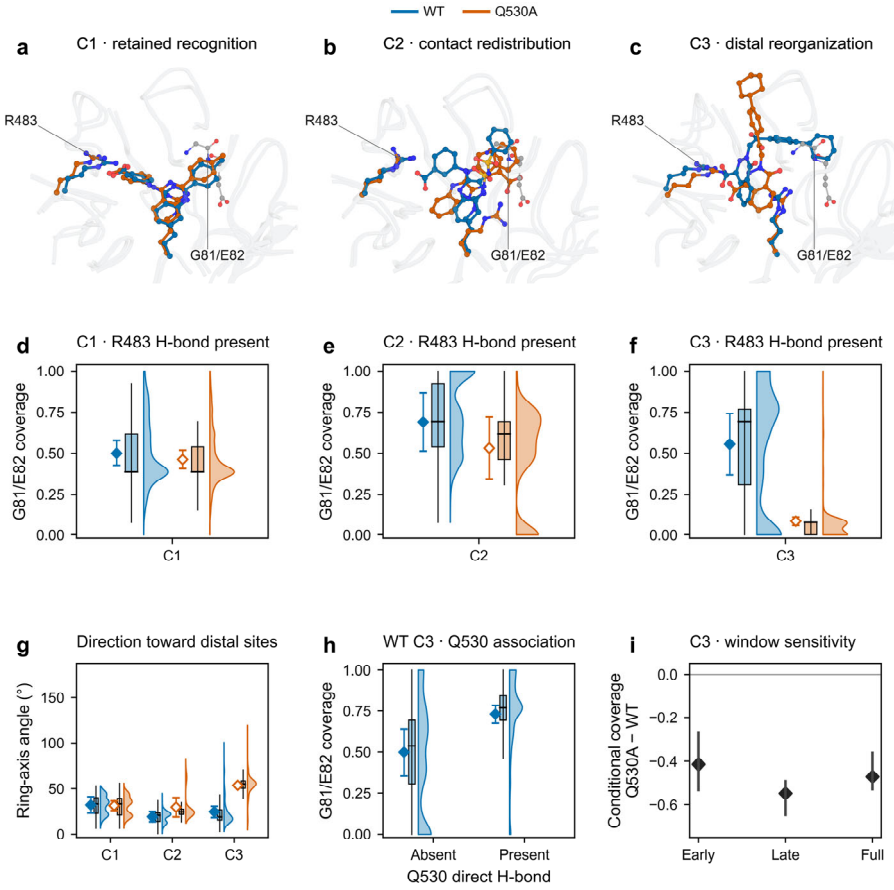


Figure 5. Ligand-dependent spatial responses and conditional distal coverage. (**a**–**c**) Representative WT (blue) and Q530A (orange) structures of C1–C3 with the gray-carbon G81/E82 portion of the ETGE reference: C2 illustrates redistribution toward R415, and C3 illustrates distal reorganization with retained R483 recognition. (**d**–**f**) G81/E82 coverage in R483-contacting frames. (**g**) Ligand-axis angle relative to the distal-reference direction in those frames. (**h**) WT C3 coverage with and without Q530 contact. (**i**) C3 conditional-coverage contrasts across early, late and full windows, with trajectory-omission ranges. Distributions use equal trajectory weights; error bars in (**d**–**h**) show between-trajectory SD ($n = 3$ per condition). C2 is shown in its simulated dianionic state.

The distal-coverage reduction persisted when the comparison was restricted to frames retaining an R483 direct hydrogen bond (Figure 5f). Mean conditional G81/E82 coverage decreased from 0.554 ± 0.188 in WT to 0.084 ± 0.026 in Q530A. Within these frames, the carboxylate-to-ring axis angle relative to the distal-reference direction increased from 24.1 ± 6.2° to 53.7 ± 1.5° (Figure 5g). The retained R483 contact thus accompanied a shift in ligand orientation away from the distal G81/E82 region. Figure S12 resolves the local contacts in the representative C1 and C3 structures.

Within WT C3, Q530-contacting frames had greater mean distal coverage than Q530-absent frames, at 0.730 ± 0.055 and 0.499 ± 0.142, respectively (Figure 5h). Q530 hydrogen-

bond occupancy was 0.416 ± 0.458 across trajectories. These configurations associate Q530 contact with the broader distal placement of C3 in the WT ensemble.

The principal C2 exclusive-contact shifts and C3 R483-conditioned coverage reduction retained their directions across the 20–100, 120–200 and 20–200 ns windows and after single-trajectory omission (Figure 5i; Figure S8). Together, the C3 observations identify a response in which local R483 recognition persists while the ligand adopts a less distal-facing orientation and occupies less of the G81/E82 reference region.

3.4. Endpoint-Energy Patterns Provide Complementary Structural Context

The endpoint-energy patterns differed among ligands and between PB and GB models (Figure 6; Table S3). C1 and C2 had small positive Q530A–WT mean contrasts with PB (+0.50 and +0.66 kcal/mol) and negative contrasts with GB (−0.80 and −1.28 kcal/mol). Between-trajectory SDs ranged from 0.89 to 4.92 kcal/mol for PB and from 1.36 to 6.99 kcal/mol for GB. For C3, PB estimates changed from −5.84 ± 6.93 kcal/mol in WT to −7.25 ± 3.75 kcal/mol in Q530A, while GB estimates changed from −30.07 ± 7.55 to −33.54 ± 6.80 kcal/mol. C3 therefore combined markedly reduced distal coverage with numerically more negative mean endpoint-energy estimates.

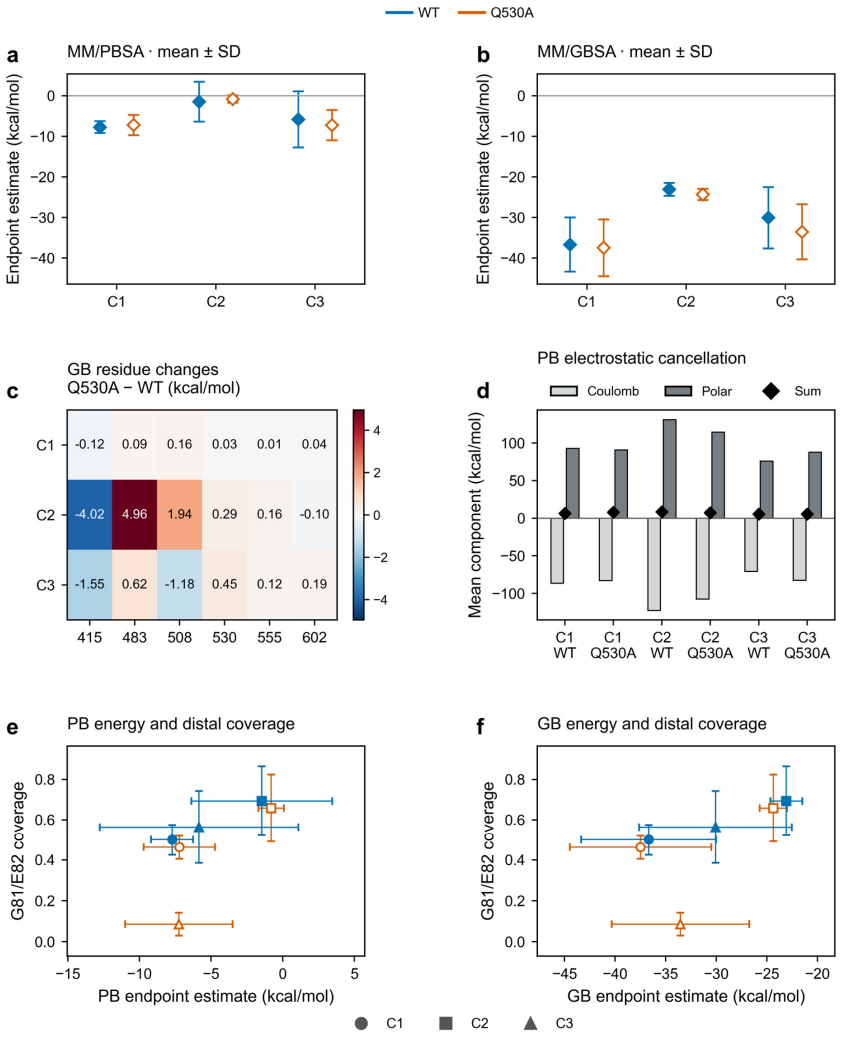


Figure 6. Endpoint-energy patterns and distal coverage. (**a**,**b**) MM/PBSA and MM/GBSA estimates. (**c**) Q530A-WT differences in GB residue contributions. (**d**) PB electrostatic and polar-solvation components. (**e**,**f**) Endpoint-energy estimates versus distal coverage. Error bars show between-trajectory SD (n = 3 trajectories per condition).

For the C2 monoanion, WT and Q530A MM/PBSA estimates were −7.00 ± 6.48 and −6.10 ± 6.59 kcal/mol, respectively; corresponding MM/GBSA estimates were −28.86 ± 3.88 and −25.88 ± 3.37 kcal/mol (Figure S16). The WT/Q530A PB difference was small relative to the between-trajectory spread, and equal-duration early and late windows showed trajectory-level variation.

C2 GB residue contributions shifted in parallel with its contact redistribution: Q530A–WT differences were −4.02 kcal/mol at R415 and +4.96 kcal/mol at R483 (Figure 6c). Electrostatic and polar-solvation components contributed opposing terms to the endpoint totals (Figure 6d). At the residue level, the energetic pattern therefore followed the exchange of recognition partners, whereas the total PB and GB estimates captured different balances among interaction components.

Time-window and trajectory-omission analyses showed greater variation in the endpoint-energy contrasts than in the principal contact and conditional-coverage patterns (Figures S7 and S8). The C3 PB mean contrast changed sign after individual trajectories were omitted, and C2′s full-window contrast differed in sign between PB and GB. The geometric reorganization and endpoint-energy patterns thus described complementary aspects of the ligand responses.

3.5. Principal KEAP1–NRF2 Interface Residues Show Sequence Conservation in Leopard Gecko

The predicted leopard-gecko KEAP1 sequence matched the modeled human segment at 243 of 285 positions (85.3%) and the predefined interface at 31 of 32 residues (Figure 1d; Figure S11; Table S5). Human R415, R483 and Q530 corresponded to gecko R383, R451 and Q498; the interface difference was human F478 versus gecko Y446. All four residues of the NRF2 ETGE motif were conserved, mapping human residues 79–82 to gecko residues 69–72. The wider reference-peptide region was identical at 13 of 16 positions. These mappings were retained across the tested gap penalties, placing the principal recognition residues within a conserved cross-species sequence context.

4. Discussion

4.1. Distinct Ligand-Dependent Modes of Recognition Reorganization

The simulations distinguish two modes of ligand reorganization at the KEAP1–NRF2 interface. Dianionic C2 exchanged its predominant local recognition partner from R483 to R415 while largely retaining mean distal coverage. C3 retained frequent R483 contact but adopted a less distal-facing orientation with markedly reduced G81/E82 coverage. C1 showed smaller changes in the same descriptors. Combining contact identities, participating functional groups and same-frame spatial coverage separates local anchoring from regional placement and explains how similar contact persistence can accompany different spatial responses.

Previous crystallographic and simulation studies established multiple ligand poses, alternative R415 orientations and hydration-sensitive recognition at KEAP1 [11–13]. The present comparison extends this framework by examining contact redistribution and regional placement under a common perturbation. Its central contribution is the distinction between exchanging local anchoring contacts and reorganizing the distal ligand region while retaining a local contact. Recent structural and biophysical work has also identified alternative binding conformations of KEAP1 ligands [29], while a separate computational screening study explored additional Kelch-domain candidates [30].

4.2. Structural Basis of the C2 and C3 Responses

For C2, ring nitrogen atoms and the deprotonated sulfonamide nitrogen supplied an alternative set of acceptors for R415. The large carboxylate shift alongside comparatively

similar mean distal coverage is consistent with reorientation of the anchoring network across the recognition surface. C3 followed a different geometry: similar carboxylate displacement accompanied a larger change in the ring-axis direction and distal coverage. The broader coverage observed in Q530-contacting WT frames supports a structural association between local polar recognition near Q530 and distal ligand placement. The monoanion simulations provide a direct sensitivity comparison. Protonation of the sulfonamide nitrogen changed its assigned donor–acceptor role and was accompanied by altered R415/R483 contact-state populations and distal reference coverage. These changes varied among trajectories and time windows. Both microstates were modeled separately and did not interconvert during simulation.

The apo response provides a protein-level background for these patterns. Q530A altered pocket geometry and increased local water access, while C2 and C3 shared the direction of the hydration change but differed in their recognition responses. Hydration is therefore part of the response around residue 530, but does not uniquely distinguish C2 from C3. Their different functional-group arrangements and directions of ligand reorientation provide the more specific structural distinction.

4.3. Relation to Endpoint Energies and Screening Context

The C2 residue contributions at R415 and R483 were consistent with the exchange of local contacts, while its total PB and GB contrasts differed in sign. C3 combined reduced distal coverage with numerically more negative mean endpoint-energy estimates, and its PB contrast was sensitive to trajectory omission. These observations place local interaction patterns, regional geometry and endpoint totals on distinct descriptive levels. Model dependence and between-trajectory variability limit quantitative affinity ranking from the endpoint estimates; the results do not establish energetic compensation.

The screening and reference comparisons further define the role of the spatial descriptors. Macrocycles 63 and 64 retained broad ETGE coverage despite different published affinities [13], and retrospective evaluation showed that geometric or pharmacophore agreement alone was insufficient to guarantee crystallographic pose recovery (Figures S9 and S10). Coverage therefore characterizes placement relative to NRF2 reference sites, rather than serving as a potency or pose-validation score. The candidates remain computational selections awaiting direct binding and competition measurements.

4.4. Scope and Limitations

The models comprise a truncated human Kelch domain, one principal force-field combination and fixed ligand microstates. Each condition shares a prepared starting structure, with three velocity-seeded 200 ns replicates; the window and omission checks assess sensitivity within that sampling and do not establish complete convergence or the exploration of alternative starting poses [24]. The two C2 microstates were modeled separately from a shared prepared heavy-atom pose; their protonation equilibrium and relative populations were not determined. Q530A changes side-chain volume, polarity and hydrogen-bond capacity together, so its response cannot be assigned to the removal of a single interaction. Velocity-seeded repeats probe variation from the shared starting structure rather than independent starting poses. The fixed-charge force fields do not explicitly represent electronic polarization, and fixed ligand microstates do not allow protonation-state interconversion during the trajectories. Force-field parameters and assigned charges may influence the local hydrogen-bond network. The 200 ns trajectories cannot establish exhaustive sampling of slower rearrangements or alternative binding modes. Protein radius of gyration remained within a narrow range in the plotted trajectories, whereas protein RMSD showed trajectory-

dependent shifts, including late increases in Q530A–C2 (Figures S1 and S2). These global profiles complement but do not establish convergence of the ligand-contact observables.

Coverage depends on the reference conformation, cutoff and ligand size; the corresponding descriptor checks are reported in Figure S5. Conditional sub-ensembles differ in size and composition, and one late-window trajectory lacked the stricter C3 R483–carboxylate state, leaving that full-cohort contrast undefined (Supplementary Methods SM4). Endpoint calculations omit entropy and use different nonpolar models for GB residue and total estimates; they are not complete binding free energies or quantitative affinity predictions. The related external docking series and repeated search seeds provide a limited retrospective comparison. Finally, the gecko sequences are predicted proteins, and sequence correspondence does not establish equivalent regulation or ligand pharmacology; no gecko functional experiment was performed. Skin-repair mechanisms therefore remain a question for subsequent biological studies.

4.5. Biological Context and Experimental Implications

Scar-free cutaneous repair in the leopard gecko provides the biological starting point [1]. Mammalian studies connect Keap1 suppression and Nrf2 perturbation to diabetic wound repair [2,3], while sustained epidermal Nrf2 activation can impair barrier homeostasis [4]. Conservation of the principal recognition residues and the ETGE motif supplies molecular context for this connection. The present structural comparison provides a focused starting point for asking how ligand recognition at KEAP1 relates to pathway responses in skin-relevant systems.

For C2, protonation-state characterization and direct binding measurements would test R415′s recognition by its nitrogen-containing region. For C3, binding and NRF2-peptide competition measurements across WT and Q530A would test the functional relevance of distal reorganization with retained local contact. Subsequent cellular or tissue studies could then relate these recognition patterns to NRF2 activity and repair phenotypes using appropriate viability and pathway controls.

5. Conclusions

Q530A revealed ligand-dependent reorganization at the KEAP1–NRF2 interface. Dianionic C2 redistributed anchoring contacts from R483 toward R415 through ring and deprotonated sulfonamide nitrogen atoms while largely retaining mean distal coverage. C3 retained local R483 recognition but showed pronounced loss of G81/E82 coverage and a shift away from the distal-reference direction. These distinct responses show that persistence of a local contact can become uncoupled from broader interface placement. Combining contact states with spatial coverage provides testable structural models for KEAP1 ligand recognition and competition. The additional monoanion simulations showed a distinct, trajectory-dependent recognition pattern.

Supplementary Materials: The following supporting information can be downloaded at https://www.mdpi.com/article/10.3390/cimb48121278/s1.

Author Contributions: Y.L.: Investigation, molecular dynamics simulations, formal analysis, and writing—original draft. J.L. (Jianlin Li): Data curation, formal analysis, and visualization. D.-Q.W.: Supervision and writing—review and editing. W.M.: Methodology, computational modeling, formal analysis, and visualization. J.L. (Jiayi Li): Conceptualization, supervision, project administration, resources, funding acquisition, and writing—review and editing. All authors have read and agreed to the published version of the manuscript.

Funding: This work was supported by the National Key R&D Program of China (2024YFA1306400) and the National Natural Science Foundation of China 32030063.

Institutional Review Board Statement: Not applicable. This computational study used public structural and published chemical/assay information and did not involve recruitment of human participants or experiments with animals.

Informed Consent Statement: Not applicable.

Data Availability Statement: The data supporting the findings of this study are provided within the article and its Supporting Information. The data presented in this study are available from the corresponding author upon reasonable request.

Acknowledgments: OpenAI Codex (powered by the GPT-6 Astra model; OpenAI, San Francisco, CA, USA) was used to assist with manuscript polishing.

Conflicts of Interest: The authors declare no conflicts of interest.

References

1. Peacock, H.M.; Gilbert, E.A.; Vickaryous, M.K. Scar-free cutaneous wound healing in the leopard gecko, *Eublepharis macularius*. *J. Anat.* **2015**, *227*, 596–610. [CrossRef]
2. Soares, M.A.; Cohen, O.D.; Low, Y.C.; Sartor, R.A.; Ellison, T.; Anil, U.; Anzai, L.; Chang, J.B.; Saadeh, P.B.; Rabbani, P.S.; et al. Restoration of Nrf2 Signaling Normalizes the Regenerative Niche. *Diabetes* **2016**, *65*, 633–646. [CrossRef]
3. Long, M.; Rojo de la Vega, M.; Wen, Q.; Bharara, M.; Jiang, T.; Zhang, R.; Zhou, S.; Wong, P.K.; Wondrak, G.T.; Zheng, H.; et al. An Essential Role of NRF2 in Diabetic Wound Healing. *Diabetes* **2016**, *65*, 780–793. [CrossRef]
4. Schäfer, M.; Farwanah, H.; Willrodt, A.H.; Huebner, A.J.; Sandhoff, K.; Roop, D.; Hohl, D.; Bloch, W.; Werner, S. Nrf2 links epidermal barrier function with antioxidant defense. *EMBO Mol. Med.* **2012**, *4*, 364–379. [CrossRef]
5. Lo, S.C.; Li, X.; Henzl, M.T.; Beamer, L.J.; Hannink, M. Structure of the Keap1:Nrf2 interface provides mechanistic insight into Nrf2 signaling. *EMBO J.* **2006**, *25*, 3605–3617. [CrossRef]
6. Horie, Y.; Suzuki, T.; Inoue, J.; Iso, T.; Wells, G.; Moore, T.W.; Mizushima, T.; Dinkova-Kostova, A.T.; Kasai, T.; Kamei, T.; et al. Molecular basis for the disruption of Keap1-Nrf2 interaction via Hinge & Latch mechanism. *Commun. Biol.* **2021**, *4*, 576. [CrossRef]
7. Marcotte, D.; Zeng, W.; Hus, J.C.; McKenzie, A.; Hession, C.; Jin, P.; Bergeron, C.; Lugovskoy, A.; Enyedy, I.; Cuervo, H.; et al. Small molecules inhibit the interaction of Nrf2 and the Keap1 Kelch domain through a non-covalent mechanism. *Bioorg. Med. Chem.* **2013**, *21*, 4011–4019. [CrossRef]
8. Ma, B.; Lucas, B.; Capacci, A.; Lin, E.Y.; Jones, J.H.; Dechantsreiter, M.; Enyedy, I.; Marcotte, D.; Xiao, G.; Li, B.; et al. Design, synthesis and identification of novel, orally bioavailable non-covalent Nrf2 activators. *Bioorg. Med. Chem. Lett.* **2020**, *30*, 126852. [CrossRef]
9. Qin, Y.; Poulsen, C.; Narayanan, D.; Chan, C.B.; Chen, X.; Montes, B.R.; Tran, K.T.; Mukminova, E.; Lin, C.; Gajhede, M.; et al. Structure-Guided Conformational Restriction Leading to High-Affinity, Selective, and Cell-Active Tetrahydroisoquinoline-Based Noncovalent Keap1-Nrf2 Inhibitors. *J. Med. Chem.* **2024**, *67*, 18828–18864. [CrossRef]
10. Lin, C.; Narayanan, D.; Barreca, M.; Poulsen, C.; da Costa, L.S.; Chen, X.; Wichman, K.G.; Charley, C.A.; Lindsay, J.L.; Dezfouli, M.; et al. Fragment-Based Drug Discovery of Novel High-affinity, Selective, and Anti-inflammatory Inhibitors of the Keap1-Nrf2 Protein-Protein Interaction. *Angew. Chem. Int. Ed.* **2025**, *64*, e202508121. [CrossRef]
11. Satoh, M.; Saburi, H.; Tanaka, T.; Matsuura, Y.; Naitow, H.; Shimozono, R.; Yamamoto, N.; Inoue, H.; Nakamura, N.; Yoshizawa, Y.; et al. Multiple binding modes of a small molecule to human Keap1 revealed by X-ray crystallography and molecular dynamics simulation. *FEBS Open Bio* **2015**, *5*, 557–570. [CrossRef]
12. Zhong, M.; Lynch, A.; Muellers, S.N.; Jehle, S.; Luo, L.; Hall, D.R.; Iwase, R.; Carolan, J.P.; Egbert, M.; Wakefield, A.; et al. Interaction Energetics and Druggability of the Protein-Protein Interaction between Kelch-like ECH-Associated Protein 1 (KEAP1) and Nuclear Factor Erythroid 2 Like 2 (Nrf2). *Biochemistry* **2020**, *59*, 563–581. [CrossRef]
13. Begnini, F.; Geschwindner, S.; Johansson, P.; Wissler, L.; Lewis, R.J.; Danelius, E.; Luttens, A.; Matricon, P.; Carlsson, J.; Lenders, S.; et al. Importance of Binding Site Hydration and Flexibility Revealed When Optimizing a Macrocyclic Inhibitor of the Keap1-Nrf2 Protein-Protein Interaction. *J. Med. Chem.* **2022**, *65*, 3473–3517. Correction in *J. Med. Chem.* **2023**, 66, 2204. [CrossRef]
14. Londhe, A.M.; Gadhe, C.G.; Lim, S.M.; Pae, A.N. Investigation of Molecular Details of Keap1-Nrf2 Inhibitors Using Molecular Dynamics and Umbrella Sampling Techniques. *Molecules* **2019**, *24*, 4085. [CrossRef]
15. Maier, J.A.; Martinez, C.; Kasavajhala, K.; Wickstrom, L.; Hauser, K.E.; Simmerling, C. ff14SB: Improving the Accuracy of Protein Side Chain and Backbone Parameters from ff99SB. *J. Chem. Theory Comput.* **2015**, *11*, 3696–3713. [CrossRef]
16. Wang, J.; Wolf, R.M.; Caldwell, J.W.; Kollman, P.A.; Case, D.A. Development and testing of a general amber force field. *J. Comput. Chem.* **2004**, *25*, 1157–1174. [CrossRef]
17. Jakalian, A.; Jack, D.B.; Bayly, C.I. Fast, efficient generation of high-quality atomic charges. AM1-BCC model: II. Parameterization and validation. *J. Comput. Chem.* **2002**, *23*, 1623–1641. [CrossRef]

18. Roe, D.R.; Cheatham, T.E., III. PTRAJ and CPPTRAJ: Software for Processing and Analysis of Molecular Dynamics Trajectory Data. *J. Chem. Theory Comput.* **2013**, *9*, 3084–3095. [CrossRef]
19. McGibbon, R.T.; Beauchamp, K.A.; Harrigan, M.P.; Klein, C.; Swails, J.M.; Hernández, C.X.; Schwantes, C.R.; Wang, L.P.; Lane, T.J.; Pande, V.S. MDTraj: A Modern Open Library for the Analysis of Molecular Dynamics Trajectories. *Biophys. J.* **2015**, *109*, 1528–1532. [CrossRef]
20. Shelley, J.C.; Cholleti, A.; Frye, L.L.; Greenwood, J.R.; Timlin, M.R.; Uchimaya, M. Epik: A software program for pKa prediction and protonation state generation for drug-like molecules. *J. Comput. Aided Mol. Des.* **2007**, *21*, 681–691. [CrossRef]
21. Wang, S.; Witek, J.; Landrum, G.A.; Riniker, S. Improving Conformer Generation for Small Rings and Macrocycles Based on Distance Geometry and Experimental Torsional-Angle Preferences. *J. Chem. Inf. Model.* **2020**, *60*, 2044–2058. [CrossRef]
22. Morris, G.M.; Huey, R.; Lindstrom, W.; Sanner, M.F.; Belew, R.K.; Goodsell, D.S.; Olson, A.J. AutoDock4 and AutoDockTools4: Automated docking with selective receptor flexibility. *J. Comput. Chem.* **2009**, *30*, 2785–2791. [CrossRef]
23. Rogers, D.; Hahn, M. Extended-connectivity fingerprints. *J. Chem. Inf. Model.* **2010**, *50*, 742–754. [CrossRef]
24. Grossfield, A.; Patrone, P.N.; Roe, D.R.; Schultz, A.J.; Siderius, D.W.; Zuckerman, D.M. Best Practices for Quantification of Uncertainty and Sampling Quality in Molecular Simulations [Article v1.0]. *Living J. Comput. Mol. Sci.* **2018**, *1*, 5067. [CrossRef]
25. Miller, B.R., III; McGee, T.D., Jr.; Swails, J.M.; Homeyer, N.; Gohlke, H.; Roitberg, A.E. MMPBSA.py: An Efficient Program for End-State Free Energy Calculations. *J. Chem. Theory Comput.* **2012**, *8*, 3314–3321. [CrossRef]
26. O'Leary, N.A.; Wright, M.W.; Brister, J.R.; Ciufo, S.; Haddad, D.; McVeigh, R.; Rajput, B.; Robbertse, B.; Smith-White, B.; Ako-Adjei, D.; et al. Reference sequence (RefSeq) database at NCBI: Current status, taxonomic expansion, and functional annotation. *Nucleic Acids Res.* **2016**, *44*, D733–D745. [CrossRef]
27. UniProt Consortium. UniProt: The Universal Protein Knowledgebase in 2025. *Nucleic Acids Res.* **2025**, *53*, D609–D617. [CrossRef]
28. Cock, P.J.; Antao, T.; Chang, J.T.; Chapman, B.A.; Cox, C.J.; Dalke, A.; Friedberg, I.; Hamelryck, T.; Kauff, F.; Wilczynski, B.; et al. Biopython: Freely available Python tools for computational molecular biology and bioinformatics. *Bioinformatics* **2009**, *25*, 1422–1423. [CrossRef]
29. Georgakopoulos, N.D.; Talapatra, S.K.; Naidu, S.D.; Dikovskaya, D.; Higgins, M.; Gatliff, J.; Nikoloudaki, R.; Schaap, M.; Walker, J.M.; Wardby, C.; et al. Tetrazole-containing naphthalene bis-sulfonamide Keap1-Nrf2 interaction inhibitors with unexpected binding modes. *Redox Biol.* **2025**, *88*, 103924. [CrossRef]
30. Hasan, M.M.; Mostaid, M.S.; Bepari, A.K.; Reza, H.M.; Hossain, M. Discovery of a novel Keap1 inhibitor for neurodegeneration through virtual screening and molecular dynamics simulations. *PLoS ONE* **2026**, *21*, e0341965. [CrossRef]

Disclaimer/Publisher's Note: The statements, opinions and data contained in all publications are solely those of the individual author(s) and contributor(s) and not of MDPI and/or the editor(s). MDPI and/or the editor(s) disclaim responsibility for any injury to people or property resulting from any ideas, methods, instructions or products referred to in the content.